Theoretical Analysis of Aircraft Afterbody Flow

George S. Deiwert* and Alison E. Andrews†
NASA Ames Research Center, Moffett Field, California
and
Kazuhiro Nakahashi‡
National Aerospace Laboratory, Tokyo, Japan

The strongly interactive flow field about aircraft afterbodies is investigated using computational techniques by which the thin-shear-layer formulation of the compressible, Reynolds-averaged Navier-Stokes equations is solved. A time-dependent implicit numerical algorithm is used to obtain solutions for a variety of afterbody and nozzle geometries, within the class of bodies of revolution for both subsonic and supersonic external flows and for sonic and supersonic underexpanded jets. Only centered nozzles with either a sharp lip or a blunt base are considered. In all cases, computed results are compared with experimental data. Turbulence closure is realized using algebraic eddy-viscosity concepts. A new and unique adaptive grid technique is used to resolve flow regimes with large gradients and to improve the accuracy and efficiency of the computational scheme. Special singular-point boundary conditions are used for similar purposes and are especially effective for highly underexpanded jets. For the cases considered, the agreement with experimental measurements is very good in inviscid-dominated regimes and qualitatively good, but less accurate, in regions where there is recirculation.

Nomenclature

C_p	= pressure coefficient
d_j	= nozzle exit diameter, calibers
D	= forebody diameter
l	= afterbody length, calibers
M	= Mach number
p	= pressure
r	= radial coordinate
Re	= Reynolds number based on diameter
T	= temperature
U,V	= contravariant velocity components
x_E	= end of afterbody
ξ,η	= curvilinear coordinates
μ_T	= turbulent viscosity coefficient
ω	= vorticity
Subscripts	
j	= jet
l	= local value
ξ,η	= differentiation with respect to ξ and η
∞	= freestream condition

Introduction

FOR many years, there has been considerable interest in understanding and predicting aircraft afterbody flows. AGARD has sponsored extensive studies through its Propulsion and Energetics Panel and Fluid Dynamics Panel. JANNAF (Joint Army, Navy, NASA, and Air Force) has sponsored similar activity through its Exhaust Plume Technology Subcommittee. These efforts, for the most part, have concentrated on experimental studies and on the development of component model predictive schemes. Since the experimental studies are quite complex and expensive, there is considerable interest in developing less expensive, yet reliable, analytical and numerical predictive schemes. Component modeling methods have enjoyed success with certain classes of flows, but when viscous-inviscid interactions are strong or when there are large regions of flow separation or recirculation or both, the assumptions in the models break down and the simulations are inadequate or, at best, suspect. In recent years, there has been an increasing effort to develop predictive methods capable of describing strongly interactive flows. Popular among these are methods solving an appropriate subset of the Navier-Stokes equations. This type of method permits capturing the interaction between the inviscid-dominated and viscous-dominated regimes (e.g., interacting shear layers). In addition, flows with regions of recirculation are naturally treated.

Holst[1] first solved the Navier-Stokes equations for supersonic flow over axisymmetric boattails with a solid-plume simulator. Mikhail[2] removed the solid-plume simulator and considered a centered propulsive jet emanating from a sharp-lipped nozzle at a Mach number of unity. Jacocks[3] treated a similar configuration with a jet, but with a subsonic external flow. Peery and Forester[4] treated multistream (concentric) nozzle flows with a transonic external flow. The nozzles had sharp lips and the jets were underexpanded. Swanson[5] used a solid-plume simulator in his study of transonic (both subsonic and supersonic) boattail flow. In all of these studies, either MacCormack's explicit[6] or his mixed[7] method was used to solve the governing finite-difference equations.

Deiwert[8] used the implicit method of Beam and Warming[9] to simulate subsonic, transonic, and supersonic, three-dimensional separated flows over axisymmetric boattailed bodies with a solid-plume simulator. Using MacCormack's method, Hasen[10] treated nozzles with blunt bases and studied the supersonic flow from an axisymmetric nozzle in a supersonic external flow. Overexpanded jets were of primary consideration, with one slightly underexpanded case included. Base pressures, flow fields, and shock structures in the jet were described in some detail. Using the implicit method,[9] Sahu et al.[11] treated the base flow of a projectile at transonic

Presented as Paper 84-1524 at the AIAA 17th Fluid Dynamics, Plasmadynamics, and Lasers Conference, Snowmass, CO, June 25-27, 1984; received Dec. 15, 1986; revision received Feb. 12, 1987.

*Chief, Aerothermodynamics Branch. Member AIAA.
†Research Scientist. Member AIAA.
‡Member AIAA.

speeds. This work was subsequently extended[12] to include base injections. Deiwert[13] and Fox[14] studied the supersonic axisymmetric flow over blunt-based afterbodies containing a supersonic centered propulsive jet. This work was extended to three dimensions[15] to treat axisymmetric configurations incident to the freestream. Nietubicz et al.[16] treated three-dimensional flows past projectile configurations at transonic speeds.

Recently, the AGARD Fluid Dynamics Committee established a working group (WG-08) to assess the state of the art of predictive capabilities for the "aerodynamics of aircraft afterbodies." As a part of this effort, a collection of experimental studies of a variety of configurations and flow conditions was gathered together to provide test data with which to evaluate predictive methods. Results of this assessment are found in Putnam and Bissinger.[17] The purpose of this paper is to present numerical results and their comparisons with experiment for some of these data, to describe the enhancements of the original Navier-Stokes scheme[13] and to assess the present predictive capability for this class of flows.

Computational Method

The computational method used has been described in some detail in Ref. 13. Briefly, the thin-layer formulation of the compressible, axisymmetric, Reynolds-averaged Navier-Stokes equations, written in generalized curvilinear coordinates, is solved in a time-marching way, using the implicit, approximate-factored finite-difference method of Ref. 9. The shear layers are constrained to lie in one principal plane, namely, the plane normal to the η coordinate.

Turbulence Closure

Turbulence closure is realized using eddy-viscosity concepts compatible with the thin-shear-layer approximation. In the present study, an algebraic model is used which is derived from the Baldwin-Lomax[18] formulation. The application of this model to aircraft afterbody flows is described in Ref. 13. This model presumes that turbulence transport is a function of the local mean flow variables only and does not contain any convective transport terms (such as are described in differential eddy-viscosity models). However, convective transport effects can be accounted for in an approximate sense using relaxation techniques (confined to the near-base region in the present study). Despite this approximation, the model has several features that make it suitable for simulating aircraft afterbody flows in which there is more than one shear layer, as will be seen in the following discussion.

The Baldwin-Lomax model is a two-layer formulation for wall-bounded shear layers. The inner layer describes the behavior in the near-wall region and is identical to the Prandtl-Van Driest formulation used in the Cebeci-Smith model. The outer layer is described by two different formulations: one to be used for attached, somewhat fully-developed shear layers and the other to be used for separated, nearly-separated, or free shear layers. A criterion for switching from one outer formulation to the other is provided for wall-bounded shear layers. The free-shear-layer formulation is used only for massively separated and free shear layers. Restricting attention now to the free-shear-layer formulation, we have

$$\mu_T = KC_{cp}F_{\text{wake}}F_{\text{Kleb}}$$

where

$$\begin{aligned}
K &= 0.0168 \text{ (Clauser's constant)} \\
C_{cp} &= 1.6 \\
F_{\text{wake}} &= C_{wk}U^2_{dif}\eta_{max}/F_{max} \\
C_{wk} &= 0.25 \\
F_{\text{Kleb}} &= [1 + 5.5(C_{\text{Kleb}}|\eta - \eta_0|/\eta_w)^6]^{-1} \\
C_{Kleb} &= 0.3 \\
U^2_{\text{dif}} &= (u^2 + v^2)_{max} - (u^2 + v^2)_{min}
\end{aligned}$$

and η_o is the location of the middle of the shear layer, U_{dif} is measured across the layer with width η_w, $F_{\max}$ is the local maximum of the function $F(\eta) = \eta|\omega|$, and $\eta_{\max}$ is the location where it occurs. Figure 1 shows a schematic illustrating the shear layers in the base region of a blunt-base aerodynamic afterbody.

It is important that the coordinate η be measured from a reference plane reasonably far away from the shear layer so that it has negligible influence on the determination of $F_{\max}$. In this way, the coordinate η drops out of the formulation entirely for free shear layers (except as it appears locally in the Klebanoff intermittency function) and yet provides for a smooth transition between the two different outer formulations for attached shear layers. If there is more than one shear layer present, as occurs in the near-base region on blunt-based afterbodies, then local extrema ($F_{\max}$ and U^2_{dif}) are identified for each layer, using the same formulation and same η-coordinate reference plane. Hence, we have a single formulation, independent of a coordinate length scale, that is applicable to flows with multiple, quasi-parallel shear layers. The length scale in these formulations is defined by $U_{\text{dif}}/|\omega|_{\max}$ and the velocity scale is defined by U_{dif}, both local quantities for distinct layers. When two shear layers begin to merge, there exists a viscous-viscous interaction that, until they blend together completely, form a complex shear layer. This complex layer is described in an approximate sense, using relaxation and averaging concepts.

In the present formulation, the essential shear layers are assumed to be aligned normal to the η-coordinate direction. In the base region of a bluff body, however, there is a wall layer that is parallel to the η coordinate. There are no viscous terms carried in the thin layer and hence no turbulence modeling treatment. Rather, a slip boundary condition is assumed with laminar flow just near the base. A transition to a turbulent flow downstream of the base is achieved by relaxing from the laminar flow at the base to a turbulent flow some distance downstream of the base (over a distance of 1 caliber). Note that the shear layers coming off the afterbody and at the jet slip surface are still described as turbulent layers. The recirculation flow in the base region, however, is quasi-laminar with a smooth transition to the bounding turbulent shear layers.

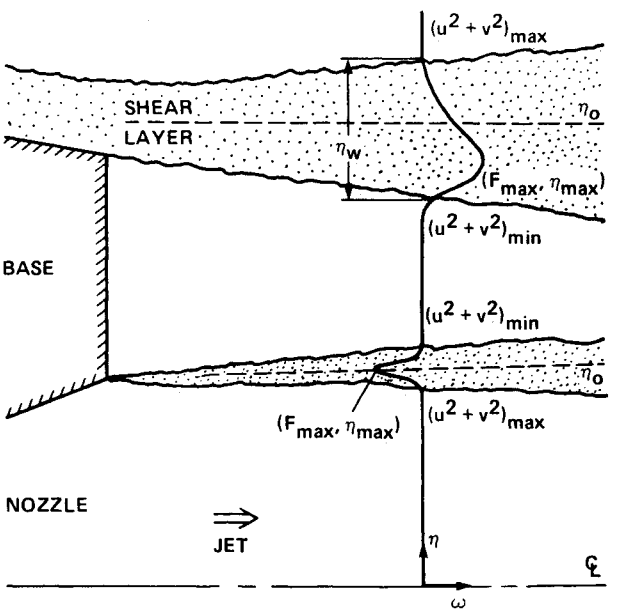

Fig. 1 Multiple free-shear-layer schematic: algebraic turbulence model.

Adaptive Grid

Flowfields over aircraft afterbodies typically are complex and contain regions of strong viscous-inviscid and strong viscous-viscous interactions. External flows are typically transonic or supersonic and contain compression shocks, as well as regions of rapid expansion. The boundary layer on the afterbody leaves as a free shear layer and merges with the shear layer between the propulsive jet and the external flow. The underexpanded propulsive jet exhibits internal structures in the form of barrel shocks and Mach disks. The locations of these high-gradient regions are not known before a flowfield solution is obtained and must be determined as part of the solution. To accurately capture and resolve these regions, it is critical to use a solution-adaptive grid. In fact, it is sometimes not possible to achieve even a stable solution without resolving regions of rapid expansion (such as near the nozzle lip) or strong compression to sufficient scale. This is particularly apparent in the case of highly underexpanded jets (static pressure ratio greater than five).

Here, the two-dimensional adaptive grid method of Nakahashi and Deiwert[19,20] is used to redistribute the grid points in order to improve the resolution in regions of high gradients and thus improve the accuracy and efficiency of the solution method. This adaptive grid method is based on variational principles that correspond to the minimization of the energy of a system of springs connecting the grid points to one another. The spring constants are determined by local gradients of the flowfield variables. Orthogonality and smoothness constraints are imposed to maintain control of the global character of the adapted grid. Directional splitting and marching concepts are used to make the method efficient and robust. It is possible to add or delete grid points at the user's discretion, thus enhancing the accuracy and efficiency of the method without increased complexity. The resulting adapted grids are effectively optimized with respect to the driving functions. In the present study, the redistribution of grid points is driven by the pressure gradient in the streamwise direction and by the density gradient in the radial direction.

Boundary Conditions

Boundary conditions for afterbody flowfield computations consist of the following:

1) No-slip, adiabatic wall, and zero normal pressure gradient on the forebody and afterbody surfaces.

2) Uniform freestream at the upstream and far-field lateral boundary.

3) Extrapolation at the downstream boundary, except for subsonic outflow conditions, for which static pressure and extrapolated density are used to determine energy from the equation of state.

4) Inviscid flow at the jet exit plane.

5) On blunt nozzle bases, slip (such that contravariant velocity component $U=0$) density and the contravariant velocity component V are extrapolated so that $p_\xi = 0$ and $V_\xi = 0$, zero normal pressure gradient is imposed, and energy is determined using the equation of state.

6) Symmetry on the upstream and downstream centerlines with zero radial gradient for mass, total momentum, and energy.

For configurations with blunt bases, there are two singular points on the base: one at the external corner and the other at the nozzle lip, denoted by points A and E, respectively, in Fig. 2. The η gradients at point A are described using boundary conditions 1 and at point E by conditions 4. The ξ gradients at both points A and E are described by extrapolating density, energy, and V; U is set to zero.

For high-pressure jets (highly underexpanded), there is a rapid expansion around the nozzle lip at point E (Fig. 2). Depending on the downstream position, different properties should be observed corresponding to the characteristic paths emanating from point E. Following the idea proposed by Fox,[14] the boundary values at point E are expanded to the line BCD for high-pressure jets (when $p_j > 5p_\infty$). A Prandtl-Meyer expansion, corresponding to the pressure at point B, is used to define properties about the point E that are then extrapolated isentropically, but with changing area, to a distribution along CD. The pressure along BC is assumed constant, the momentum components and energy are interpolated between B and C, and the density is determined by the equation of state. The location of point C along line BD is determined as a function of the flowfield solution — namely, by the turning angle corresponding to the computed pressure at point B to which the jet can expand. The pressure at point B is determined as described for points A and E, since there is insufficient information to determine the pressure at point B using the normal momentum equation. This expanded treatment of the nozzle lip at point E permits the efficient treatment of very-high-pressure jets, imposes correct physical behavior, and stabilizes the solution procedure.

Computed Cases

A set of six afterbody/flowfield combinations are considered for comparison with experimental data. These cases, summarized in Table 1, are among those selected by the

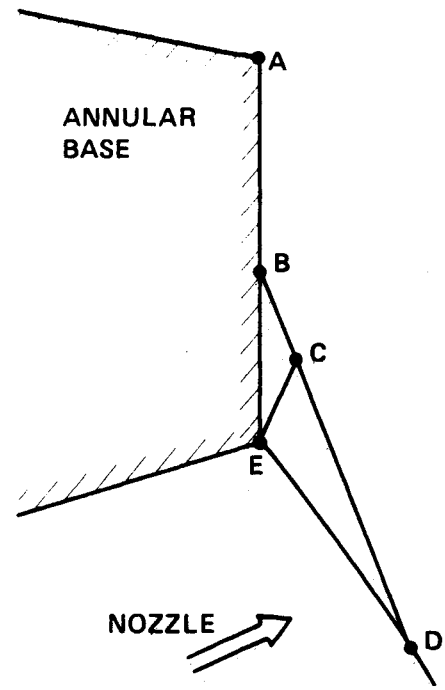

Fig. 2 Base boundary singular points.

Table 1 Afterbody and flowfield combinations

Case	Geometry	M_∞	M_j	p_j/p_∞	l	d_j	T_j/T_∞
1	Circular arc	0.8	1.0	1.532	1.768	0.5	1.0
2	Circular arc	0.8	1.0	1.532	0.8	0.5	1.0
3	Cylinder	2.01	2.5	1.0	0.0	0.6	1.0
4	Cylinder	2.01	2.5	6.0	0.0	0.6	1.0
5	Cylinder	2.01	2.5	1.0	1.0	0.6	1.0
6	Cylinder	2.01	2.5	6.0	1.0	0.6	1.0

AGARD Fluid Dynamics Committee Working Group (WG-08) to assess the state of the art of our predictive capability for the "aerodynamics of aircraft afterbodies."

In the first two cases, subsonic flow over circular arc boattails with choked flow emanating from sharp-lipped nozzles is considered. Cases 1 and 2 were tested extensively at NASA Langley and are described in Refs. 21-25. The freestream Mach number is 0.8, the jet exit Mach number is unity, and the nozzle pressure ratio is 1.532. The case 1 afterbody is 1.768 calibers long with a base diameter of 0.5 caliber. This case was designed to support fully attached flow over the afterbody at these flow conditions. The case 2 afterbody is 0.8 calibers long with a base diameter of 0.5 caliber. This configuration leads to separated flow over the afterbody.

Both cases were simulated assuming a 14 deg half-angle conical nose and cylindrical forebody, which was the experimental configuration. The computational region was discretized with 140 points in the streamwise direction and 68 points in the radial direction, 20 of which are distributed across the jet exit plane. As described in previous studies,[8,13,15] stretching and clustering of grid point distributions was used extensively to focus resolution in the boundary layer and near corners. In addition, the grid point distributions, which were initially distributed using algebraic methods, were adapted to the solution several times during the course of the development of the solutions.

Shown in Figs. 3 and 4 are computed and experimentally measured surface pressure coefficient distributions over the afterbodies of the first two cases. The agreement between computation and experiment for these cases is excellent, except over the long separation bubble in case 2. In the separated flow region (see Fig. 4), the simulated distribution fails to indicate a pressure plateau and somewhat overpredicts the pressure recovery and, hence, underpredicts the afterbody pressure drag. This suggests inaccurate prediction of boundary-layer displacement thicknesses over the separated flow region (a separation bubble that is too thin) and points directly to weaknesses in the turbulence model in this regime. Swanson[5] shows that better agreement can be achieved in this region using a global relaxation turbulence model. It is of interest to note, however, that the present predicted location of separation agrees remarkably well with experimental results for case 2. Separation was also predicted for case 1, but only near the end of the afterbody. No experimental data evidenced this separation, probably because of a lack of instrumentation or flow visualization in this region sufficient to detect flow reversal so close to the end of the afterbody.

Shown in Fig. 5 are comparisons of computed and experimental local flow angles over the afterbodies of cases 1 and 2. Plotted at six different radial positions away from the centerline is local flow angle variation with streamwise distance. Away from the body, the agreement between computation and experiment is excellent. Near the body surface and downstream, the measured oscillations in flow angle are not captured computationally. This may be due to numerical dissipation or insufficient grid resolution in the streamwise direction.

Figure 6 shows comparisons of computed and experimental local Mach numbers over the afterbodies of cases 1 and 2. Plotted in the same format as the local flow angle is the difference between the local Mach number and the freestream Mach number ($\Delta M = M_l - M_\infty$). Again, the agreement between computation and experiment is good, but with some discrepancy near the afterbody surface and near the free shear layer. Here, the computed results indicate a lower Mach number (less full boundary-layer profile) than the experimental data. Some of this discrepancy might be attributable to experimental probe interference effects near the afterbody surface, but more probably the major difference is primarily a result of improper turbulence transport modeling in regions of adverse pressure gradient. As in the previous plot, the ΔM plot also shows that the physical oscillations in the shear layer have not been accurately described by the computation.

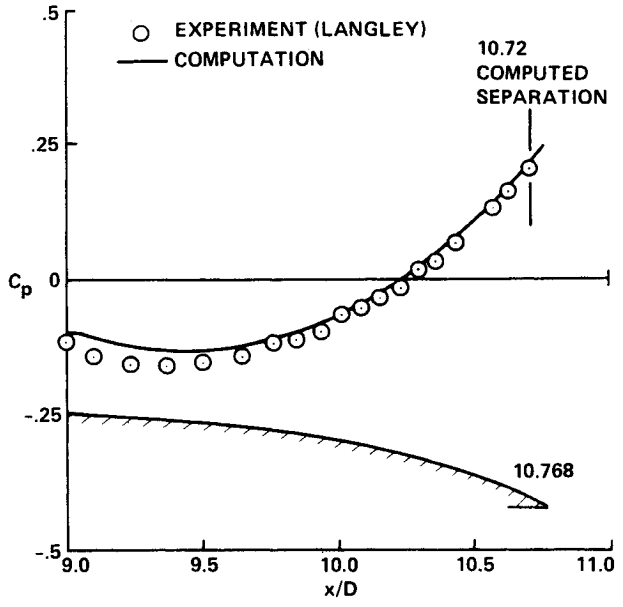

Fig. 3 Afterbody surface pressure coefficient distributions, case 1 ($M_\infty = 0.8$, $M_j = 1.0$, $p_j/p_\infty = 1.532$, $l = 1.768$).

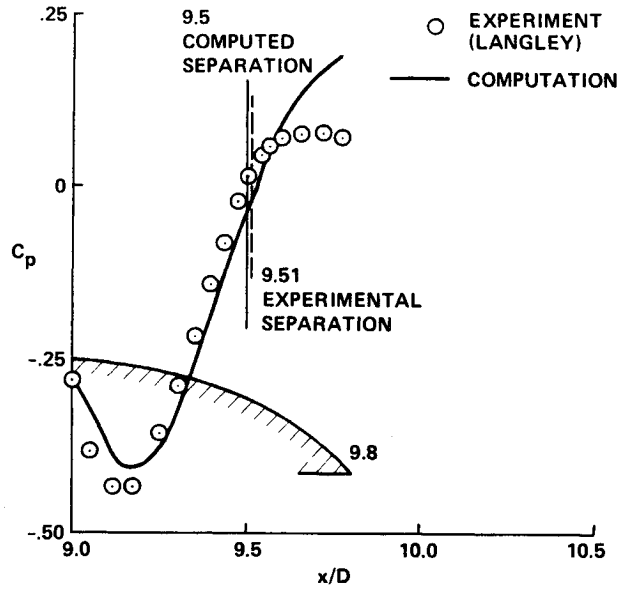

Fig. 4 Afterbody surface pressure coefficient distributions, case 2 ($M_\infty = 0.8$, $M_j = 1.0$, $p_j/p_\infty = 1.532$, $l = 0.8$).

Turning now to the flowfield structure in the jet and the interaction between the jet and the external flow, we have shown in Fig. 7 computed and measured pitot pressure profiles at seven streamwise positions downstream of the nozzle exit for both cases 1 and 2. The agreement for case 1 (Fig. 7a) is excellent, both in jet spreading rate and in the details of streamwise expansion and recompression near the jet centerline. The agreement for case 2 (Fig. 7b) is also good, but there are minor differences in jet spreading and in the details of jet expansion and recompression near the centerline. The difference in jet spreading is somewhat influenced by differences in the shear layers coming off the afterbody surface.

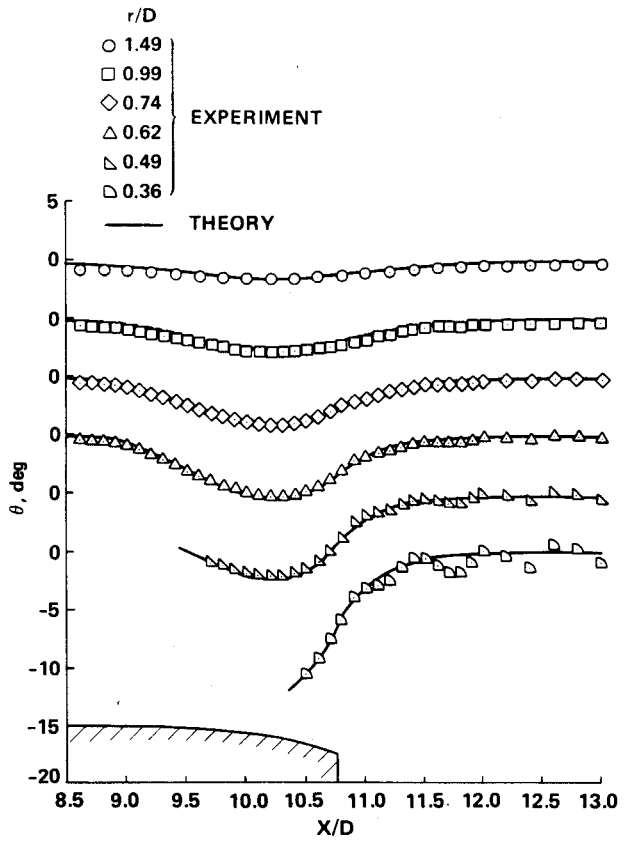

a) Case 1.

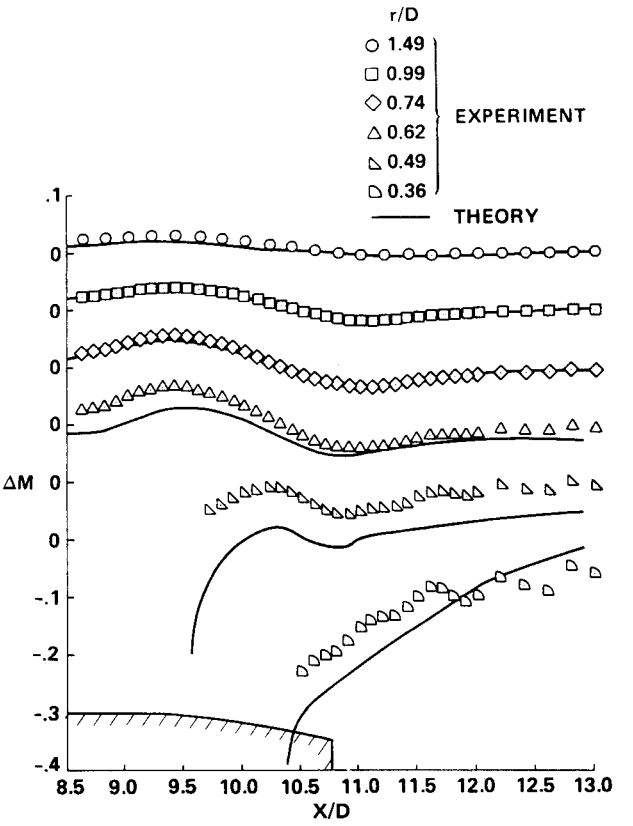

a) Case 1.

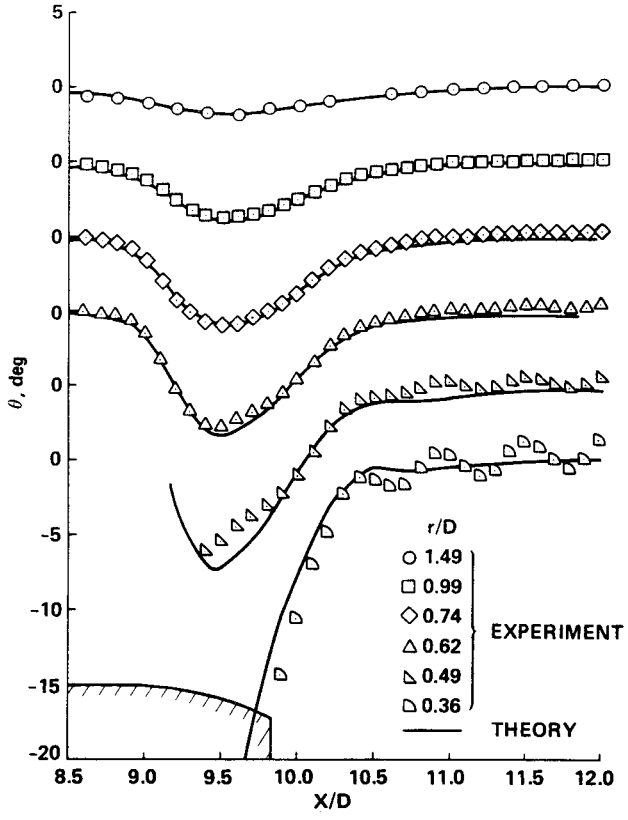

b) Case 2.

Fig. 5 Computed and measured local flow angle.

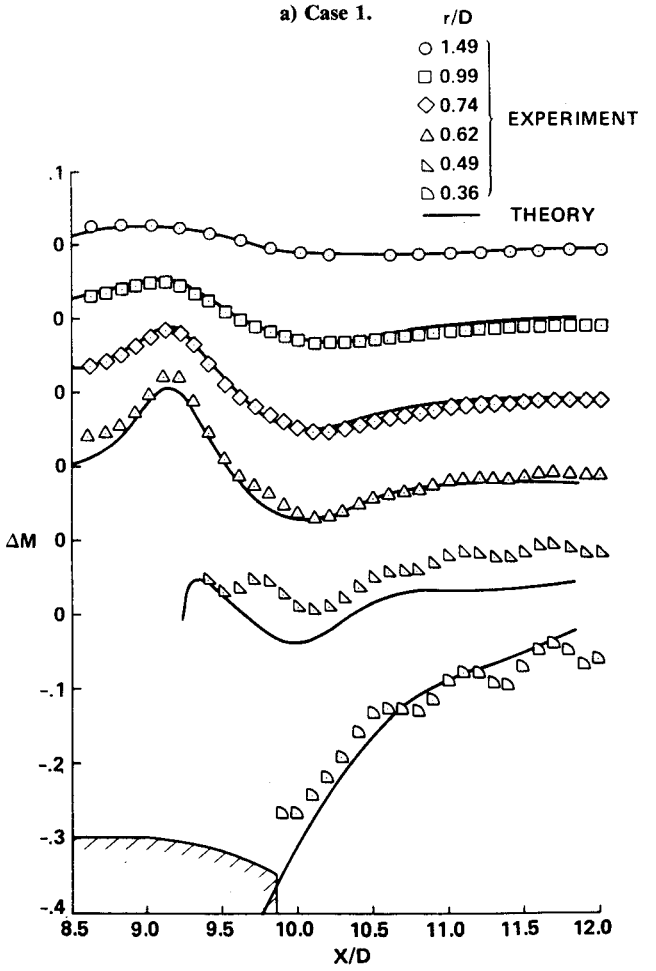

b) Case 2.

Fig. 6 Computed and measured local Mach number ($\Delta M = M_1 - M_\infty$).

a) Case 1 ($x_E/D = 10.768$).

b) Case 2 ($x_E/D = 9.80$).

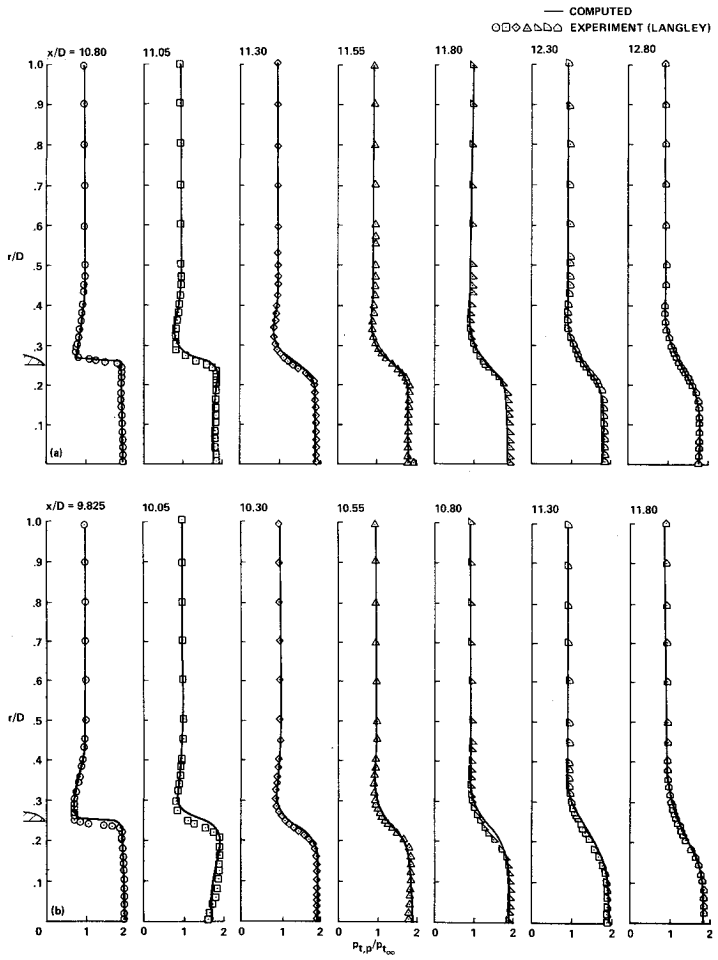

Fig. 7 Pitot pressure profiles in jet.

A general observation concerning prediction of displacement effects is that in regions of adverse pressure gradient, the displacement thickness is generally overpredicted when the boundary layer is attached. When the boundary layer separates, however, the thickness of the separation bubble is underpredicted. This leads to underprediction of pressure level for attached layers after an adverse pressure gradient and overprediction when the flow has separated. Possible causes for underprediction of displacement thickness for attached layers include 1) insufficient resolution around expansion corners (see, e.g., Ref. 8); 2) grid dependency near solid surfaces (adaptive gridding was not used in wall-bounded shear layer regions); and 3) lack of adverse pressure gradient correction terms in the turbulent transport model. The underprediction of separation bubble thickness is certainly a result of using eddy viscosity coefficients in the reverse flow region that are too large.

The remaining cases 3-6 have supersonic flow past a blunt-base afterbody containing a centered propulsive jet at Mach 2.5. Cases 3 and 4 have a straight cylindrical afterbody with jet-to-freestream pressure ratios of 1 and 6, respectively. Cases 5 and 6 have 6 deg conical afterbodies, 1 caliber long, and again have pressure ratios of 1 and 6, respectively. These configurations have been tested extensively by Agrell and others (see Refs. 26–28).

Figure 8 shows the initial algebraically generated grid in the near-base region that was used for cases 3 and 4. There is initial clustering of the radial lines near the end of the afterbody and clustering of the streamwise lines near the afterbody shear layer and near the jet exit shear layer. This grid contains 113 points in the streamwise direction and 100 points in the radial direction, with 20 points across the jet exit plane and 33 across the blunt base. This grid was adapted to the flow three times during the course of the solution, based on density gradient in the radial direction and pressure gradient in the streamwise direction, for both cases. Shown in Fig. 9 are the final grids used for these cases. Twenty-two grid points have been added in the streamwise direction in each of the cases to help define the region containing the Mach disk near the jet centerline. This brings the total number of grid points in the streamwise direction to 135. Computed Mach contours for these cases are shown in Fig. 10 and they clearly indicate the locations of the oblique compression shocks, jet mixing layer, barrel shock, and Mach disk. These high-gradient regions have, for the most part, been adequately captured and resolved. There is still room for improvement in the resolution of the Mach disk and the precise axial location of the disk is somewhat sensitive to this resolution.

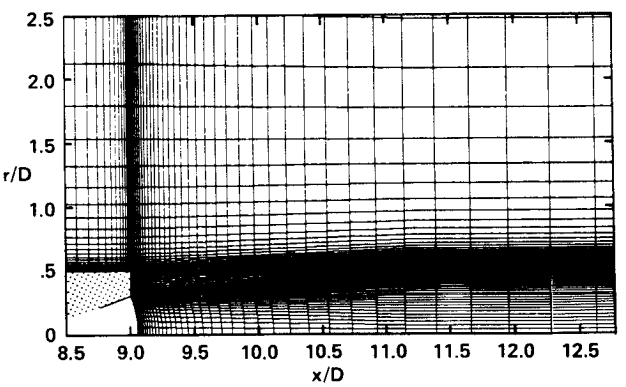

Fig. 8 Initial grid in base region: cases 3 and 4.

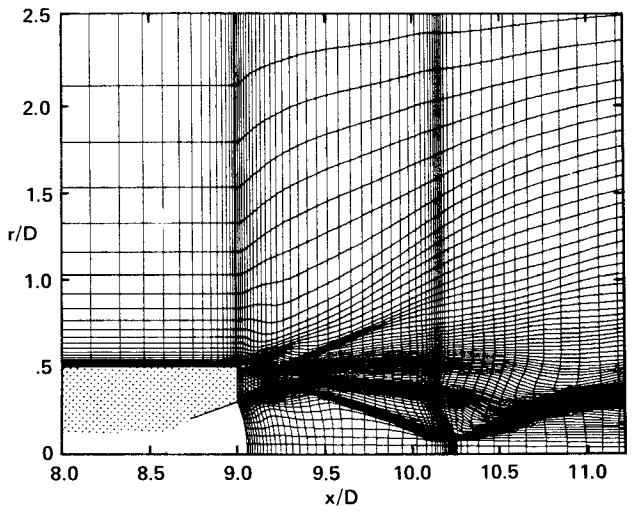

a) Case 3 ($p_j = p_\infty$).

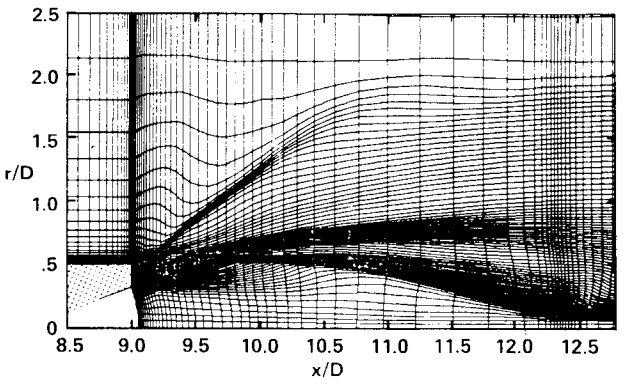

b) Case 4 ($p_j = 6p_\infty$).

Fig. 9 Final adapted grid in base region.

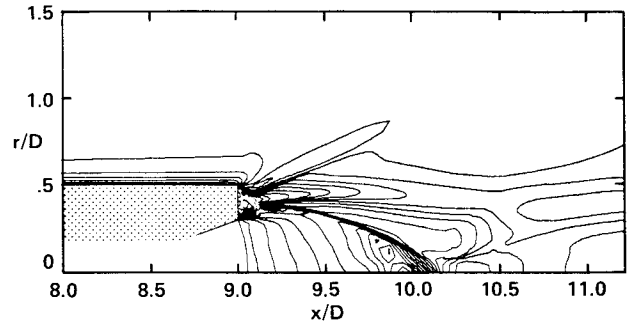

a) Case 3 ($p_j = p_\infty$).

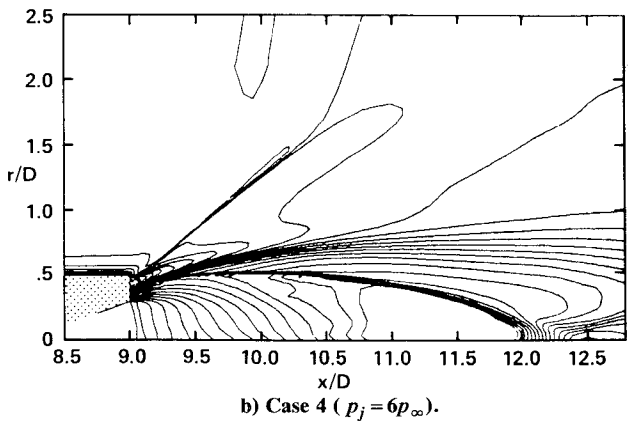

b) Case 4 ($p_j = 6p_\infty$).

Fig. 10 Computed Mach contours in base region ($M_\infty = 2.0$, $M_j = 2.5$).

Figure 11 shows comparisons of computed density contours and isobars with schlieren photographs obtained under like experimental flow conditions. The photographs were provided by Johan Agrell and the Flygtekniska Försöksanstalten, the Aerodynamic Research Institute of Sweden, where the experimental tests were performed. Critical lines corresponding to shocks, shear layer boundaries, and contact discontinuities have been traced from the photographs and superimposed on the computed contours. The agreement between computation and experiment is excellent, with some minor variation being noted in the location of the Mach disks. In cases 4 and 5, the oblique lambda shock just off the end of the afterbody has been accurately simulated. This is not true for case 6, how-

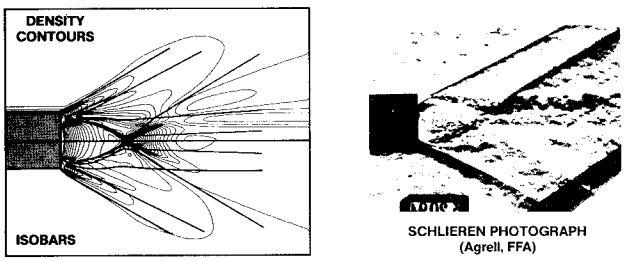

a) Case 3, cylindrical afterbody ($p_j = p_\infty$).

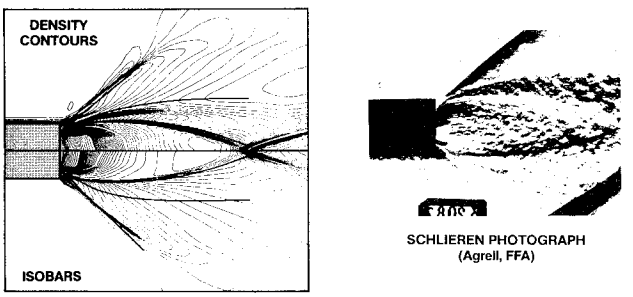

b) Case 4, cylindrical afterbody ($p_j = 6p_\infty$).

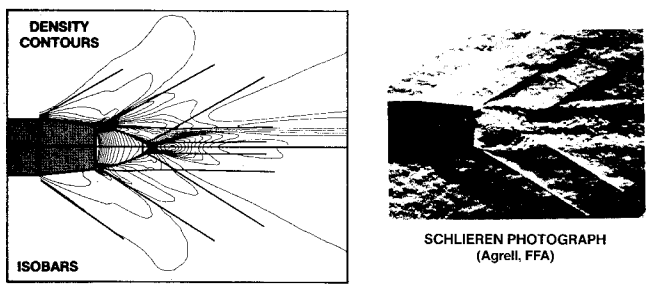

c) Case 5, conical afterbody ($p_j = p_\infty$).

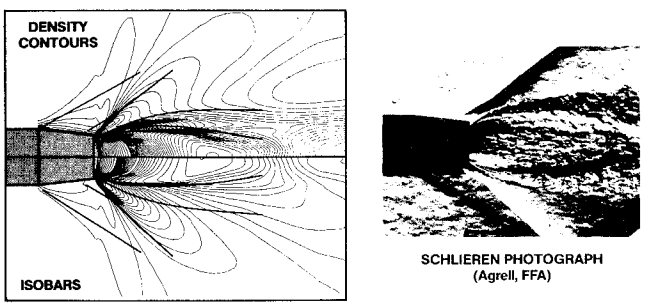

d) Case 6, conical afterbody ($p_j = 6p_\infty$).

Fig. 11 Computed density contours and isobars in base region compared with schlieren photograph for afterbody with centered jet.

ever, where experimental evidence indicates an interaction between the upstream leg of the lambda shock and the boundary layer on the afterbody. This kind of shock/boundary-layer interaction is not observed computationally until the jet exit pressure is increased further. The onset of this type of interaction seems to occur, for this particular geometry, for jet-to-freestream pressure ratios near 6. It is this onset that is not predicted computationally rather than the phenomenon itself.

Conclusions

It has been demonstrated that it is possible to simulate, in considerable detail, the complex flow features associated with a variety of aerodynamic afterbody shapes and a variety of flow conditions. Comparisons with experimental data show these simulations to be reasonably accurate. Such computations, although not sufficient to compute overall drag for any given configuration accurately enough for design purposes, can be valuable in performing parametric studies and for looking at flowfield structures. The solutions are quite good in inviscid-dominated regimes. Although quantitative comparisons of shock strength and location have not been made, comparison of schlieren photographs and computed contours does show qualitatively accurate prediction of shock location and structure in the exhaust plume and external flowfield. The regions of viscous-inviscid interaction seem to be generically correct, but are less precise. And the regions of flow recirculation, although captured and defined, are probably imprecise in their detail.

Two critical areas can be identified where improvement is necessary. The first is in modeling the turbulence transport mechanism in the base flow region and for interacting free shear layers. It seems important for flows with large recirculating regions to include convective effects in the turbulence transport mechanism and to try to define a length scale in a realistic manner. The second area is in the treatment of boundary conditions for large base regions and the inclusion of additional shear terms in the equations (i.e., the thin-layer approximation used in the present study is not valid near the base). For afterbodies with small base regions, such as configurations used in cases 5 and 6, this is probably not so critical. But for large bases, the error can be large.

The use of solution-adaptive grids has been advantageous in strategically repositioning grid points as complex flow features emerge during a computation. Although it is always desirable to have as much resolution as possible, the adaptive grid procedure can put the points that are available in optimal positions. A further nontrivial advantage in using an adaptive grid is in simplifying grid generation. It is practical to use simple and efficient algebraic initial grid generation procedures, or even to use grids from some other solution for a like geometry, and to develop an efficient optimal grid as the solution evolves.

References

[1]Holst, T.L., "Numerical Solution of Axisymmetric Boattail Fields with Plume Simulators," AIAA Paper 77-0224, 1977.

[2]Mikhail, A.G., "Computation of a Supersonic Flow Field Past an Axisymmetric Nozzle Boattail with Jet Exhaust," AIAA Paper 78-0993, 1978.

[3]Jacocks, J.L., "Computation of Axisymmetric Separated Nozzle-Afterbody Flow," AEDC-TR-79-71, 1980.

[4]Peery, K.M. and Forester, C.K., "Numerical Simulation of Multi-Stream Nozzle Flows," AIAA Paper 79-1549, 1979.

[5]Swanson, R.C. Jr., "Numerical Solutions of the Navier-Stokes Equations for Transonic Afterbody Flows," NASA TP-1784, Dec. 1980.

[6]MacCormack, R.W. and Baldwin, B.S., "A Numerical Method for Solving the Navier-Stokes Equations with Applications to Shock-Boundary Layer Interactions," AIAA Paper 75-1, 1975.

[7]MacCormack, R.W., "An Efficient Numerical Method for Solving the Time-Dependent Compressible Navier-Stokes Equations at High Reynolds Number," *Proceedings of the ASME Winter Annual Meeting*, ASME, New York, 1976, pp. 49-64.

[8]Deiwert, G.S., "Numerical Simulation of Three-Dimensional Boattail Afterbody Flowfields," AIAA Paper 80-1347, 1980 (also *AIAA Journal*, Vol. 19, May 1981, pp. 582-588).

[9]Beam, R. and Warming R.F., "An Implicit Finite-Difference Algorithm for Hyperbolic Systems in Conservation-Law Form," *Journal of Computational Physics*, Vol. 22, Sept. 1976, pp. 87-110.

[10]Hasen, G.A. "Navier-Stokes Solutions for an Axisymmetric Nozzle," *AIAA Journal*, Vol. 20, Sept. 1982, pp. 1219-1227.

[11]Sahu, J., Nietubicz, C.J., and Steger, J.L., "Numerical Computation of Base Flow for a Projectile at Transonic Speeds," AIAA Paper 82-1358, 1982.

[12]Sahu, J., Nietubicz, C.J., and Steger, J.L., "Navier-Stokes Computations of Projectile Base Flow with and without Base Injection," AIAA Paper 83-0224, 1983 (also *AIAA Journal*, Vol. 23, Sept. 1985, pp. 1348-1355).

[13]Deiwert, G.S., "A Computational Investigation of Supersonic Axisymmetric Flow over Boattails Containing a Centered Propulsive Jet," *AIAA Journal*, Vol. 22, Oct. 1984, pp. 1358-1365.

[14]Fox, J.H., "Predicting Plume-Induced Separation on Bluff-Base Bodies," AIAA Paper 84-0315, 1984.

[15]Deiwert, G.S. and Rothmund, H. "Three-Dimensional Flow over a Conical Afterbody Containing a Centered Propulsive Jet: A Numerical Simulation," AIAA Paper 83-1709, 1983.

[16]Nietubicz, C.J., Mylin, D.C., Sahu, J., and Lafarge, R., "Aerodynamic Coefficient Predictions for a Projectile Configuration at Transonic Speeds," AIAA Paper 84-0326, 1984.

[17]Putnam, L.E. and Bissinger, N.C., "Results of AGARD Assessment of Prediction Capabilities for Nozzle Afterbody Flows," AIAA Paper 85-1464, July 1985.

[18]Baldwin, B.S. and Lomax, H., "Thin Layer Approximation and Algebraic Model for Separated Turbulent Flows," AIAA Paper 78-0257, 1978.

[19]Nakahashi, K. and Deiwert, G.S., "A Practical Adaptive Grid Method for Complex Fluid Flow Problems," NASA TM-85989, 1984.

[20]Nakahashi, K. and Deiwert, G.S., "A Self-Adaptive-Grid Method with Application to Airfoil Flow," AIAA Paper 85-1525, 1985.

[21]Reubush, D.E. and Runckel, J.F., "Effect of Fineness Ratio on Boattail Drag of Circular-Arc Afterbodies Having Closure Ratios of 0.50 with Jet Exhaust at Mach Numbers up to 1.30," NASA TN D-7192, 1973.

[22]Abeyounis, W.K. and Putnam, L.E., "Investigation of the Flow Field Surrounding a Circular-Arc Boattail Nozzle at Subsonic Speeds," NASA TP-1633, 1980.

[23]Mason, M.L. and Putnam, L.E., "Pitot Pressure Measurements in Flow Fields Behind Circular-Arc Nozzles with Exhaust Jets at Subsonic Free-Stream Mach Numbers," NASA TM-80169, 1979.

[24]Abeyounis, W.K., "Boundary-Layer Separation on Isolated Boattail Nozzles," NASA TP-1226, 1979.

[25]Reubush, D.E. and Putnam, L.E., "An Experimental and Analytical Investigation of the Effect on Isolated Boattail Drag of Varying Reynolds Number up to 130×10^6," NASA TN D-8210, 1976.

[26]Agrell, J. and White, R.A., "An Experimental Investigation of Supersonic Axisymmetric Flow over Boattails Containing a Centered Propulsive Jet," Flygtekniska Försöksanstalten, Stockholm, Sweden, FFA Tech. Note AU-913, 1974.

[27]Addy, A.L. and White, R.A., "Optimization of Drag Minimum Including Effects of Flow Separation," *Transactions of ASME, Journal of Engineering for Industry*, Vol. 95, No. 1, Feb. 1973, pp. 360-364.

[28]Addy, A.L., "Thrust-minus-drag Optimization by Base Bleed and/or Boattailing," *Journal of Spacecraft and Rockets*, Vol. 7, Nov. 1970. pp. 1360-1362.